Measuring masses in low mass X-ray binaries via X-ray spectroscopy: the case of MXB 1659-298

Gabriele Ponti[1], Stefano Bianchi[2], Teo Muñoz-Darias[3,4] and Kirpal Nandra[1]
[1] *Max-Planck-Institut für Extraterrestrische Physik, Giessenbachstrasse, D-85748, Garching, Germany*
[2] *Dipartimento di Matematica e Fisica, Università degli Studi Roma Tre, Via della Vasca Navale 84, I-00146, Roma, Italy*
[3] *Instituto de Astrofísica de Canarias, 38205 La Laguna, Tenerife, Spain*
[4] *Departamento de astrofísica, Univ. de La Laguna, E-38206 La Laguna, Tenerife, Spain*

28 June 2018

ABSTRACT
The determination of fundamental parameters in low-mass X-ray binaries typically relies on measuring the radial velocity curve of the companion star through optical or near-infrared spectroscopy. It was recently suggested that high resolution X-ray spectroscopy might enable a measurement of the radial velocity curve of the compact object by monitoring the Doppler shifts induced by the orbital motion of the disc wind or the disc atmosphere. We analysed a *Chandra*-HETG+*NuSTAR* soft state observation of MXB 1659-298, an eclipsing neutron star low-mass X-ray binary (LMXB). We measured a radial velocity curve whose phase offset and semi-amplitude are consistent with the primary star. We derived the value for the semi-amplitude of the radial velocity for the compact object $K_1 = 89 \pm 19$ km s^{-1}, constrained the mass of the secondary ($0.3 \leqslant M_2 \leqslant 0.8$ M$_\odot$) and the orbital inclination of the binary system ($73 \leqslant i \leqslant 77^\circ$). These values are consistent with previous estimates from independent methods. Via the same technique, the next generation of X-ray observatories equipped with high spectral resolution instruments (e.g., *Athena*) will have the potential to measure the radial velocity curve of the primary in high inclination X-ray binaries to an accuracy of a few per cent.

Key words: Neutron star physics, X-rays: binaries, absorption lines, accretion, accretion discs, methods: observational, techniques: spectroscopic

1 INTRODUCTION

Dynamical masses of black holes and neutron stars (NS) in X-ray binaries (XRB) can be derived through phase-resolved photometric and spectroscopic campaigns in the optical or the near infrared (nIR; Cowley et al. 1992; Charles & Coe 2006, Casares & Jonker 2014). This is achieved by measuring the Doppler motion and rotational broadening of the absorption lines generated at the photosphere of the companion star. These quantities provide, under the assumption of co-rotation, a determination of the mass function, the mass ratio and the binary orbital inclination (e.g. Casares & Jonker 2014). Decades of optical-nIR spectroscopic studies have demonstrated the power of these techniques to determine the masses of compact objects, however they are limited to sources with relatively bright companion stars in quiescence or the presence of fluorescence lines from the donor in outburst (Steeghs & Casares 2002; Muñoz-Darias et al. 2005). However, often the semi-amplitude of the radial velocity of the compact object (K_1) remains elusive. Though, K_1 is fundamental to obtain a dynamical solution, whenever the mass ratio of the two stars cannot be determined, and it is of great value for searches of continuous gravitational waves (Watts et al. 2008).

It was recently proposed an alternative technique to determine the mass of compact objects, based on high spectral resolution X-ray spectroscopy (Zhang et al. 2012). This method relies on measuring orbital shifts in the observed energies of absorption lines from disc winds or disc atmospheres, since these are expected to trace the motion of the compact object around the centre of mass of the binary system (i.e. K_1). This technique has been already applied to a few black hole and NS systems (Zhang et al. 2012; Madej et al. 2014). However, it was concluded that the variability of either the source luminosity or random variations of the wind outflow speed can severely affect the accurate determination of the orbital motion of the compact object (Madej et al. 2014). In addition, for typical low-mass X-ray binaries (LMXB), the expected radial velocity of the primary is of the order of $K_1 \sim 10 - 150$ km s^{-1}, therefore beyond the energy resolution of current X-ray instruments in the Fe K band, where the strongest absorption lines are present (Ponti et al. 2012; Diaz-Trigo et al. 2013).

Here, we report on the determination of the radial velocity curve of the primary in MXB 1659-298. This was achieved by applying the method proposed by Zhang et al. (2012) to several absorption lines in the soft X-ray band, where current X-ray instruments provide the highest energy resolution. MXB 1659-298 is a transient LMXB displaying type-I X-ray bursts, therefore indi-

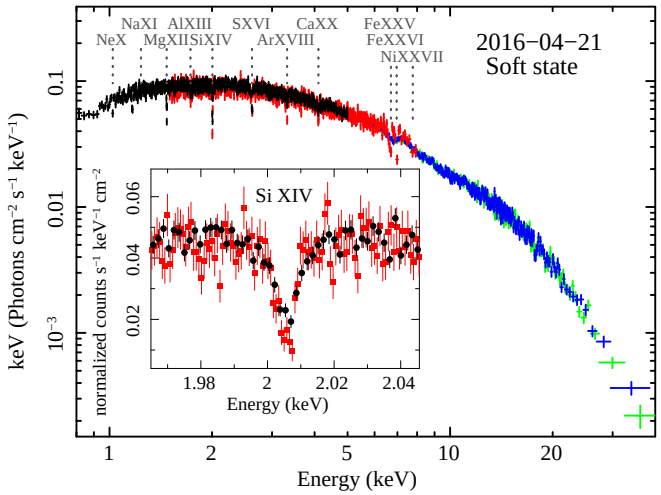

Figure 1. *Chandra*+*NuSTAR* spectra of MXB 1659-298, accumulated on 2016-04-21. The black, red, green and blue points show the MEG, HEG, FPMA and FPMB mean spectra, respectively. As is typical for the soft state, the spectra are best fitted with an absorbed disk black-body, a black-body and a Comptonisation component (Ponti et al. in prep). Additionally, more than 60 absorption lines are detected, signatures of an additional ionised absorption component (the strongest Lyα lines detected are indicated, as well as the Fe XXV line). The inset shows a zoom into the Si XIV Lyα line.

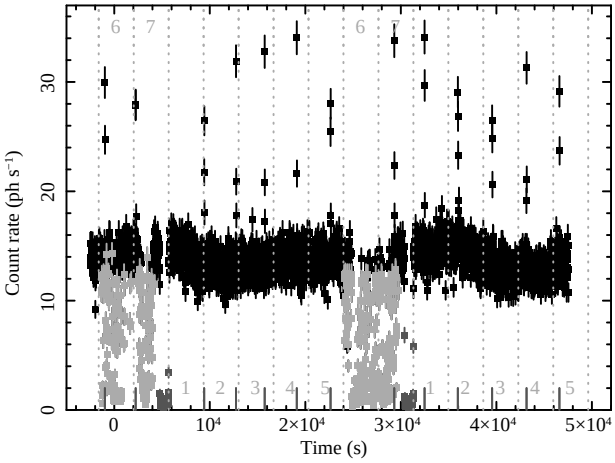

Figure 2. First order *Chandra* HETG light curves of MXB 1659-298 (14.9 s time bins). Intense dipping activity (light grey) is observed, primarily before the two eclipses (dark grey). Thirteen bursts are also observed (affected by pile up at the burst peaks). The grey dotted vertical lines indicate the intervals used for the phase resolved study, while the solid lines at the bottom indicate the occurrence time of the bursts.

cating a neutron star primary (Lewin et al. 1976; Galloway et al. 2008). It is a high inclination system, showing dipping and eclipsing events, with an orbital period of $P_{orb} = 7.1$ hr and an eclipse duration of ≈900 s (Cominsky 1984; Jain et al 2017; Iaria al 2018).

The optical counterpart of MXB 1659-298 was found to have $V \sim 18$ during outburst (Doxsey et al. 1979) and to display orbital brightness variations as well as narrow eclipses (Wachter et al. 2000). The optical spectrum during outbursts is rather typical for a LMXB, with a blue continuum, He II and Bowen blend emission but no spectral features from the donor (Canizares et al. 1980; Shahbaz et al. 1996). During quiescence, MXB 1659-298 is very faint with $V > 23$ (Cominsky et al. 1983), $R = 23.6 \pm 0.4$ and $I = 22.1 \pm 0.3$ (Filippenko et al. 1999; Wachter et al. 2000). Assuming a reddening of $E_{B-V} = 0.3$ (van Paradijs & McClintock 1995) and based on the observed $(R - I)_0 = 1.2$ and the empirical period-mass relation, Wachter et al. (2000) suggested that the companion star is an early K to early M main sequence star.

MXB 1659-298 started a new outburst on August 2015 (Negoro et al. 2015). LMXB observed at high inclination, such as MXB 1659-298, are known to display strong ionised absorption during the soft state, associated with an equatorial wind or the disc atmosphere (Diaz-Trigo et al. 2006; Ponti et al. 2012). Therefore, in order to perform the first high energy resolution study of the ionised absorber in MXB 1659-298, we triggered *Chandra* and simultaneous *NuSTAR* observations.

2 ANALYSIS

The *NuSTAR* (Harrison et al. 2013) observation (obsid 90201017002) started on 2016-04-21 at 14:41:08 UT. The data were reduced with the standard *nupipeline* scripts v. 0.4.5 and the high level products produced with the *nuproducts* tool. The *Chandra* spectra (obsid 17858 on 2016-04-21 13:44:43 UT) and response matrices have been produced with the CHANDRA_REPRO task, combining the positive and negative first orders. The light curve was extracted with the DMEXTRACT task. Bursts were singled out by visually inspecting the *Chandra* and *NuSTAR* light curves and selecting intervals of enhanced emission (typically lasting ≈ 100 − 200 s; Fig. 2).

Figure 1 shows the mean *Chandra* and *NuSTAR* spectra. As hoped, we caught the source during the soft state. The simultaneous spectra show, in addition to the typical soft state continuum, an array of more than 60 absorption lines. The absorption lines are due to highly ionised plasma (Ponti et al. in prep). The strongest lines are labeled in Fig. 1 and they correspond to the Lyα transitions (as well as the Fe XXV line) of the most abundant elements. The broad band continuum can be fit by the sum of a disk black-body ($kT_{DBB} \approx 1.1 - 1.5$ keV), black-body ($kT_{BB} \approx 2.5 - 3.0$ keV) and a Comptonisation component, all absorbed by neutral material ($N_H \approx 1.5 - 2.1 \times 10^{21}$ cm^{-2}; for more details Ponti et al. in prep).

Figure 2 shows the first order *Chandra* light curve. Two eclipses are detected, preceded by intense dipping activity. By fitting the eclipse transitions, we determined the eclipse center with an accuracy of seconds ($P_{\rm orb}$=25.618 ks, consistent with previous results; Jain et al. 2017; Iaria et al. 2018). We first divided the dataset into intervals of 3659.7 s, so that 7 intervals cover an entire orbital period. The start of the first interval is chosen so that it begins just after the end of the eclipse (see grey dotted lines in Fig. 2; we define as phase 0 the eclipse center). We then removed the periods affected by bursts and eclipses. This resulted in a shorter cleaned exposure for the 7^{th} interval, because of the presence of the eclipses. We then extracted the HEG and MEG first order spectra corresponding to the first intervals after the eclipses (accumulating the spectra over both orbital periods), and so forth.

3 PHASE DEPENDENT ABSORPTION VARIATIONS

We started by simultaneously fitting the HEG and MEG spectra within a narrow energy band ($\Delta\lambda/\lambda \approx 0.06$) centred on the absorption feature under consideration. We applied this process for the four strongest soft absorption lines: Mg XII Lyα ($\lambda_0 = 8.4210$ Å); Si XIV Lyα (6.1822); S XVI Lyα (4.7292) and Ar XVIII

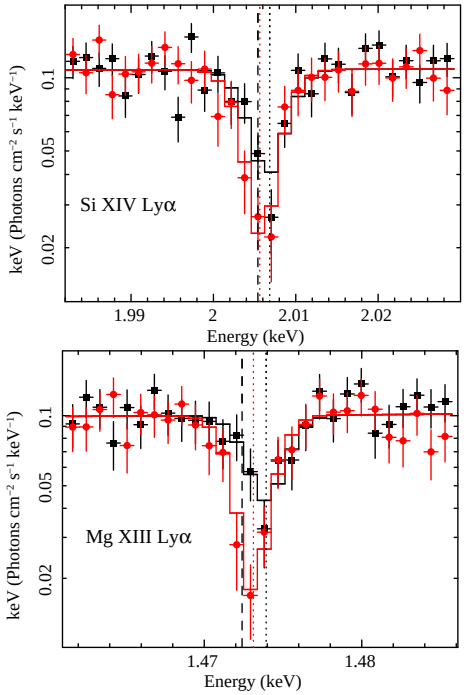

Figure 3. *(Top panel)* Black squares, red circles and solid lines show the MEG spectra and best fit models at the energy of the Si XIV line, accumulated during phase 0.02-0.16 and 0.59-0.73, respectively. The dotted lines indicate the best fit Gaussian line energies, while the dashed line show the expected line transition. *(Bottom panel)* Spectra and best fit models around the Mg XII transition, accumulated during phase 0.16-0.31 and 0.31-0.45, respectively. The vertical lines carry the same meaning as the top panel.

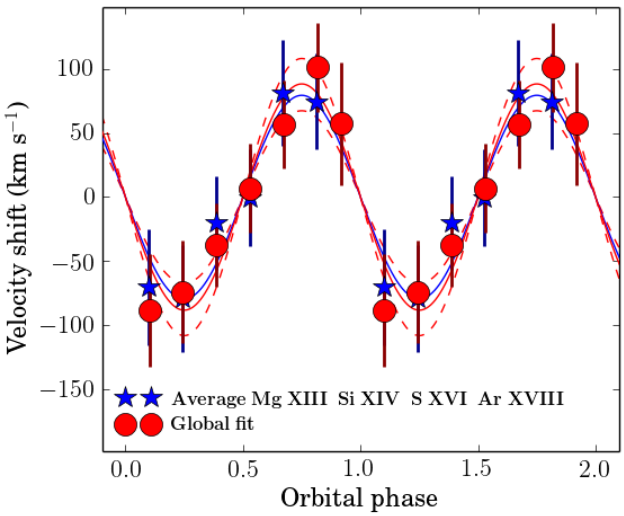

Figure 4. The blue stars and red dots show the average velocity shift for the Mg XII Lyα, Si XIV Lyα, S XVI Lyα and Ar XVIII Lyα lines and for all the lines, respectively (1-σ statistical errors). The lines appear red-shifted at phase $\approx$0.25 and blue-shifted at $\approx$0.75, as expected by the movement of the NS around the centre of mass of the binary. The blue and red lines show the best fit with a sinusoid for the average four lines (K_1=80$\pm$22 km s^{-1}) and all the lines (K_1=89 $\pm$ 19 km s^{-1}), respectively. The red dashed lines indicate the 1-sigma uncertainties on the best fit model. An offset smaller than the instrument calibration (γ=$-$49 km s^{-1}) has been subtracted off.

Lyα (3.7329 Å)[1]. We fitted the continuum with the best fit model of the mean *Chandra+NuSTAR* spectra, leaving only the normalisation of the disk black-body component and the column density of the neutral absorber free to vary as a function of phase[2].

Figure 2 shows that the spectra during interval 6 and 7 are affected by intense dipping activity. Dipping is typically generated by an increased column density of low ionisation absorption, causing a drop of the soft X-ray continuum flux (Sidoli et al. 2001; Boirin et al. 2004; Diaz-Trigo et al. 2006). This effect is captured in our narrow band fits by either an increase in the column density of the neutral absorber or a drop of the normalisation of the continuum (e.g., during interval 6). Because of the presence of the dips and the shorter cleaned exposure, we do not consider interval 7 here.

We independently fitted each strong absorption line as a function of phase (e.g., from interval 1 to 6; phases 0.02 to 0.88). We performed this by adding to the continuum a Gaussian absorption profile, with energy and intensity of the line free to vary as a function of phase (after verifying that the line width was consistent with being constant). For all lines, we observed that the line centroid energies showed a larger blue shift in the first part of the orbit, compared with later on (e.g., see Fig. 3). To measure the amplitude and significance of this effect, we recorded for each of the strongest soft X-ray lines the velocity shift and its error, as a function of phase. The blue stars in Fig. 4 show, as a function of phase, the weighted average of the observed shifts for the four strongest soft lines (Mg XII; Si XIV; S XVI and Ar XVIII). A fit with a constant velocity provides a best fit value of $\gamma = -48$ km s^{-1} and a $\chi^2 = 14.2$ for 5 dof. We then added to the model a sinusoid component with free amplitude and zero-phase (φ_0; the period was assumed to be unity). The best fit yielded $\varphi_0 = 0.54 \pm 0.05$, consistent with an orbital modulation induced by the motion of the primary (φ_0=0.5). Therefore, we re-fitted the data leaving only the semi-amplitude (i.e. K_1) as free parameter (i.e. fixing φ_0=0.5). This significantly improved the fit ($\Delta\chi^2 = 12.7$ for the addition of one parameter, corresponding to a $\approx 3\sigma$ improvement). The observed best fit values are: $\gamma = -49\pm16$ km s^{-1} and $K_1 = 80\pm22$ km s^{-1} (Fig. 4)[3]. The observed γ might, in theory, trace a bulk outflow velocity of the ionised plasma, such as a wind, or be related with the systemic velocity of MXB 1659-298. However, the absolute wavelength accuracy of the HEG is $\pm$0.006 Å, corresponding to $\approx$ 140 km s^{-1} at 1 keV ($\sim$ 3 times larger than γ), therefore, we do not discuss γ any further.

To improve the determination of the velocity shift, we built a self-consistent photo-ionisation model (IA$_{\rm soft}$). The model table was computed with CLOUDY 17.00 (Ferland et al. 2013), providing as input the observed soft state spectral energy distribution, constant electron density $n_e = 10^{14}$ cm^{-3}, turbulent ve-

[1] The reported wavelengths correspond to the average of the wavelengths of the respective doublets (Mg XII: 8.4192, 8.4246; Si XIV: 6.1804, 6.1858; S XVI: 4.7274, 4.7328; Ar XVIII: 3.7311, 3.7365 Å), weighted over the oscillator strength. We repeated the analysis and we considered two Gaussian lines for the doublets, obtaining the same results.

[2] We note that, due to the small energy band considered, a similar result is obtained by fitting the phase resolved spectra with a simple power law, with free normalisation only.

[3] To estimate the uncertainties on the best fit parameters, we simulated 10^5 radial velocity curves where each value of the velocity is due to a randomisation of the observed velocity assuming a normal distribution with a width as large as its observed uncertainty. Then, for each randomisation, we computed the best fit sinusoidal function. Finally, from the envelope of 10^5 best fit functions, we determined the uncertainties on the best fit parameters from the lower 15.9 and upper 84.1 percentiles on the envelope of the functions.

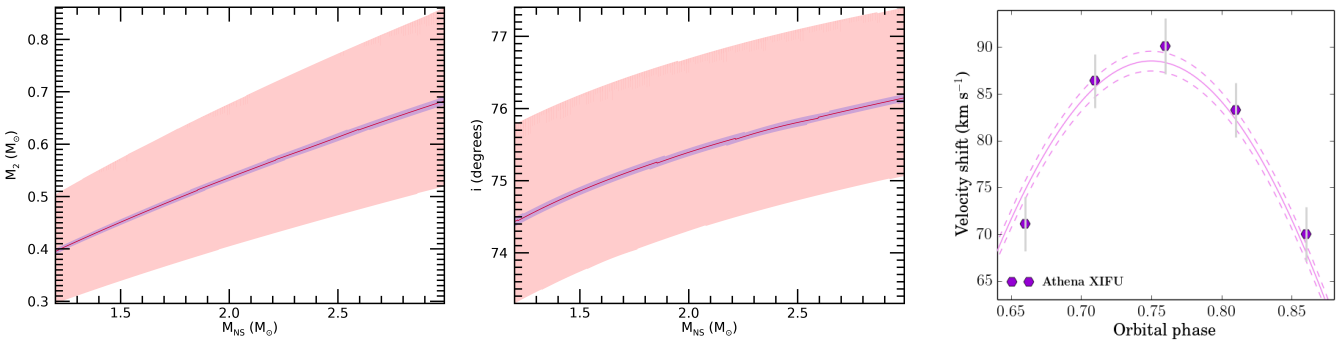

Figure 5. *(Left and center panels)* Constraints on the orbital inclination (i), NS (M_{NS}) and companion star masses (M_2) derived from the mass function (eq. 1) and the eclipse duration (eq. 3), under the assumption that the companion star fills its Roche lobe (eq. 4). The pink and violet areas show the region allowed by the current and future (*Athena*) uncertainties. *(Right panel)* Determination of the semi-amplitude of the radial velocity curve through a 100 ks *Athena* XIFU observation. A zoom on a small part of the radial velocity curve is shown, in order to exhibit the small uncertainties. K_1 will be precisely constrained to ($K_1 = 89.0 \pm 0.9$ km s^{-1}).

locity $v_{turb} = 500$ km s^{-1} and Solar abundances (for more details see Ponti et al. in prep). We then fitted the phase resolved spectra, over the entire usable energy range (0.8-6 keV for MEG and 1.2 -7.3 keV for HEG). The advantage of this global fit, compared with the independent fit of each single line, is that the energy separation between the different absorption lines is set by the atomic physics in the model. We fitted the spectra with a disk black-body (DISKBB) plus black-body (BBODY) model absorbed by neutral (TBABS) plus ionised material (in XSPEC jargon: TBABS*IA$_{\rm soft}$*(DISKBB+BBODY); Arnaud 1996), with all parameters free to vary[4]. The red points in Fig. 4 show the best fit velocity shift, as a function of phase. We note that the consideration of the full array of absorption lines led to results fully consistent with those obtained by analysing only the four strongest lines and to slightly reduce the error bars on the radial velocity measurement.

The fit with a constant could be rejected ($\chi^2 = 21.3$ for 6 dof). The fit significantly improved by adding a sinusoidal component[5] ($\Delta\chi^2 = 19.3$ for the addition of one parameter, corresponding to $\sim 3.5\sigma$ improvement), producing an acceptable fit ($\chi^2 = 2.0$ for 5 dof). The best fit yielded $K_1 = 89 \pm 19$ km s^{-1} (see red solid and dashed lines in Fig. 4). The HEG relative wavelength accuracy is ± 0.001 Å, corresponding to ≈ 25 km s^{-1} at 1 keV, comparable to the statistical uncertainties on the velocity shift at each orbital phase. Therefore, our measurement of K_1 is solid.

4 DISCUSSION

Direct measurements of K_1 have been possible for the case of X-ray binary pulsars, where the delay in the arrival time of the pulses accurately trace the orbit of the primary and therefore K_1. As an alternative, we used the absorption lines from ionised material likely formed in the atmosphere of the inner accretion disc. Since they arise from a confined region surrounding the compact object they are expected to trace its motion around the centre of mass of the binary (Zhang et al. 2012). The measured φ_0 of the sinusoidal radial velocity curve corroborates this picture. Likewise, one can compare the derived $K_1 = 89 \pm 19$ km s^{-1} with that determined in other NS LMXB with similar orbital periods and inclinations. We observed that our K_1 measurement is very similar to those derived in these other systems. Indeed, both the eclipsing LMXB X-ray pulsar X1822-371 (orbital period $P_{\rm orb} = 5.6$ hr; Hellier & Mason 1989) and EXO 0748-676 ($P_{\rm orb} = 3.8$ hr; Parmar et al. 1986) have $K_1 = 94.5 \pm 0.5$ km s^{-1} and $K_1 = 100 \pm 20$ km s^{-1}, respectively (Jonker & Van der Klis 2001; Muñoz-Darias et al. 2009; although the latter value is derived from optical data via diagnostic diagrams therefore less accurate; Shafter et al. 1986). On the contrary, black holes and low-inclination NS systems have typically significantly smaller K_1 values (e.g. Casares & Jonker 2014). Since both the phase offset and velocity amplitude derived from the absorption lines energy shifts are consistent with tracing the motion of the NS, they can be used to constrain some of the fundamental parameters of MXB 1659-298.

4.1 Constraints on the NS mass and the orbital inclination

The measured radial velocity curve of the NS allowed us to derive the mass function of the system:

$$\frac{K_1^3 P_{orb}}{2\pi G} = \frac{M_2^3 sin^3 i}{(M_{NS} + M_2)^2}, \quad (1)$$

where M_{NS} and M_2 are the NS and the companion star masses, G the Gravitational constant and i the orbital inclination. This equation sets the first constraint on the unknowns: M_{NS}, M_2 and i.

The knowledge that the eclipse duration lasts $\Delta T_{ecl} = 899.1 \pm 0.6$ (Iaria et al. 2017) adds an additional constraint. Indeed, following Iaria et al. (2017), we have computed the size of the occulted region x (see fig. 5 in Iaria et al. 2017) as:

$$x = \frac{\pi a \Delta T_{ecl}}{P_{orb}}, \quad (2)$$

where a is the orbital separation ($a^3 = \frac{G(M_{NS}+M_2)}{4\pi}$). This allowed us to constrain i as a function of M_{NS} and M_2:

$$tan^2(i) = \frac{R_2^2 - x^2}{a^2 - (R_2^2 - x^2)}, \quad (3)$$

where R_2 is the companion star radius, by assuming that the secondary star is filling its Roche lobe ($R_2 = R_L$; Paczyński 1971):

$$R_2 = R_{L2} = 0.462 a \left(\frac{M_2}{M_{NS} + M_2}\right)^{1/3}. \quad (4)$$

By applying these two constraints to the three unknowns, we estimated that, for any reasonable NS mass ($1.2 \leqslant M_{NS} \leqslant 3\,M_\odot$), the companion star mass should lie within the range $0.3 \leqslant M_2 \leqslant$

[4] Thanks to the better determination of the continuum allowed by the broad band fit, we included also interval 7 to this analysis.

[5] The best fit phase resulted to be 0.01 ± 0.04, therefore we re-fitted the data, fixing the phase to be equal to 0 in the fit.

$0.8\,M_\odot$ and the orbital inclination $73 \leqslant i \leqslant 77^\circ$ (Fig. 5). The measured ranges of the most likely companion star masses and orbital inclinations are consistent with previous methods (Wachter et al. 2000). This demonstrates that it is possible to constrain the fundamental parameters of MXB 1659-298 with current X-ray data and that this method can be applied to other systems.

4.2 Limitations and relevance of the method

The technique employed here presents also limitations. For example, it requires the presence of a further constraint (e.g., via optical-nIR observations; Casares & Jonker 2014), in order to eliminate the degeneracy between the orbital inclination and the masses of the two stars. Additionally, it assumes that the bulk motion of either the accretion disc wind or of the ionised disc atmosphere is azimuthally symmetric and constant during the orbit. Despite this assumption appears reasonable at first approximation, second order effects might be present. For example, the wind outflow velocity might vary, implying that the radial velocity curve should be averaged over several orbital periods. Besides, the wind/atmosphere is likely structured into a multi-phase plasma, characterised by different physical parameters, possibly complicating the analysis. Additionally, the wind/atmosphere kinematic might be perturbed by the material transferred from the companion star or by the presence of disc structures (e.g., eccentric discs; strong warps).

Currently the main limitation is due to the large statistical uncertainties on the determination of the radial velocity curve. However, the next generation of X-ray spectrographs/calorimeters will mend this state of affairs. Indeed, compared with HETG, *XARM* and *Athena* will improve the resolving power and the figure of merit for weak line detections at 6 keV, by a factor of ≈ 6, ≈ 12 and ≈ 8, ≈ 40, respectively, while *Arcus* at 1.5 keV will improve it by ≈ 3 and ≈ 7, respectively (Nandra et al. 2013; Kaastra et al. 2016; Gandhi 2018). We also note that this method can be applied to any LMXB displaying ionised absorption lines produced by the disc atmosphere/wind. This category comprises the majority of the high inclination LMXB (about half of the sample) during their softer states (Diaz-Trigo et al. 2006; Ponti et al. 2012).

4.3 The power of *Athena*-XIFU to constrain masses

To measure the power of future X-ray spectroscopy to constrain the mass function of MXB 1659-298, we simulated an *Athena*-XIFU 100 ks observation (assuming the "as proposed" version of the response matrix with reduced effective area, to preserve excellent spectroscopy at high throughput; Barret et al. 2016). We assumed the same observed flux ($F_{0.5-10\,keV} = 9.5 \times 10^{-10}$ erg cm^{-2} s^{-1}), spectral continuum and ionised plasma parameters as measured during the *Chandra* observation (Ponti et al. in prep). We further assumed that the ionised plasma is affected by the radial velocity curve of the primary, as observed. Figure 5 demonstrates that *Athena* observations will allow us to determine the amplitude of the radial velocity curve with an uncertainty of $\approx$1 %. The blue curves in Fig. 5 show the constraints that such an observation will allow us to deliver, translating into an uncertainty of $\approx$5 % on the mass of the primary, would the radial velocity of the companion star be known (e.g., via optical spectroscopy). Therefore, future X-ray missions will be able to deliver measurements of the radial velocity of LMXB to an accuracy of a few per cent.

ACKNOWLEDGMENTS

The authors wish to thank Fiona Harrison, Karl Forster and the *Chandra* team for approving the *NuSTAR* DDT and quickly scheduling the simultaneous observations. The authors also wish to thank Eugene Churazov, Joachim Trümper and Florian Hofmann for discussion. GP acknowledges financial support from the Bundesministerium für Wirtschaft und Technologie/Deutsches Zentrum für Luft- und Raumfahrt (BMWI/DLR, FKZ 50 OR 1604, FKZ 50 OR 1715) and the Max Planck Society. SB acknowledges financial support from the Italian Space Agency under grants ASI-INAF I/037/12/0 and 2017-14-H.O. TMD acknowledges support by the Spanish MINECO via a Ramón y Cajal Fellowships (RYC-2015-18148), the grant AYA2017-83216-P and the EU COST Action CA16214 (STSM reference number: 40355).

REFERENCES

Arnaud, K. A. 1996, Astronomical Data Analysis Software and Systems V, 101, 17
Barret, D., Lam Trong, T., den Herder, J.-W., et al. 2016, Proc. SPIE, 9905, 99052F
Boirin, L., Parmar, A. N., Barret, D., Paltani, S., & Grindlay, J. E. 2004, A&A, 418, 1061
Canizares, C. R., McClintock, & Grindlay 1980, ApJ, 236, L55
Casares, J., & Jonker, P. G. 2014, SSRv, 183, 223
Charles, A., & Coe 2006, Compact stellar X-ray sources, 39, 215
Cominsky, L., Ossmann, & Lewin, W. H. G. 1983, ApJ, 270, 226
Cominsky, L. R., & Wood, K. S. 1984, ApJ, 283, 765
Cowley, A. P. 1992, ARA&A, 30, 287
Díaz Trigo, M., Parmar, A. N., Boirin, L., Méndez, M., & Kaastra, J. S. 2006, A&A, 445, 179
Díaz Trigo, M., & Boirin, L. 2013, Acta Polytechnica, 53, 659
Doxsey, R., Bradt, H., Johnston, M., et al. 1979, ApJ, 228, L67
Ferland, G. J., Porter, R. L., van Hoof, P. A. M., et al. 2013, RMxAA, 49, 137
Filippenko, A. V., Leonard, Matheson, et al. 1999, PASP, 111, 969
Galloway, D. K., Muno, M. P., Hartman, J. M., Psaltis, D., & Chakrabarty, D. 2008, ApJS, 179, 360-422
Gandhi, P. 2018, Nature Astronomy, 2, 434
Harrison, F. A., Craig, Christensen, et al. 2013, ApJ, 770, 103
Hellier, C., & Mason, K. O. 1989, MNRAS, 239, 715
Jain, Paul, Sharma, Jaleel, & Dutta 2017, MNRAS, 468, L118
Jonker, P. G., & van der Klis, M. 2001, ApJ, 553, L43
Kaastra, J. S. 2017, Astronomische Nachrichten, 338, 146
Iaria, R., Gambino, Di Salvo, et al. 2018, MNRAS, 473, 3490
Lewin, W. H. G., Hoffman, J. A., Doty, J., & Liller, W. 1976, IAU circular, 2994, 2
Madej, O. K., Jonker, P. G., Díaz Trigo, M., & Miškovičová, I. 2014, MNRAS, 438, 145
Muñoz-Darias, T., Casares, & Martínez-Pais 2005, ApJ, 635, 502
Muñoz-Darias, Casares, O'Brien, et al. 2009, MNRAS, 394, L136
Nandra, K., Barret, D., Barcons, X., et al. 2013, arXiv:1306.2307
Negoro, H., Furuya, K., Ueno, S., et al. 2015, ATEL, 7943,
Paczyński, B. 1971, ARA&A, 9, 183
Parmar, A. N., White, Giommi, & Gottwald 1986, ApJ, 308, 199
Ponti, G., Fender, Begelman, et al. 2012, MNRAS, 422, L11
Shafter, A., Szkody, P., & Thorstensen, J. 1986, ApJ, 308, 765
Shahbaz, T., Smale, Naylor, et al. 1996, MNRAS, 282, 1437
Sidoli, L., Oosterbroek, T., Parmar, A. N., Lumb, D., & Erd, C. 2001, A&A, 379, 540
Steeghs, D., & Casares, J. 2002, ApJ, 568, 273
van Paradijs, J., & McClintock, J. E. 1995, X-ray Binaries, 58
Wachter, S., Smale, A. P., & Bailyn, C. 2000, ApJ, 534, 367
Watts, A. L., Krishnan, B., Bildsten, L., & Schutz, B. F. 2008, MNRAS, 389, 839
Zhang, S.-N., Liao, J., & Yao, Y. 2012, MNRAS, 421, 3550